

Study of the Structural and Electronic Properties of Neutral and Charged Niobium-Doped Silicon Clusters: Niobium Encapsulated in Silicon Cages

Xin Xin Xia,^{†,‡} Andreas Hermann,[§] Xiao Yu Kuang,^{*,†} Yuan Yuan Jin,[†] Cheng Lu,^{*,‡,||} and Xiao Dong Xing[†]

[†]Institute of Atomic and Molecular Physics, Sichuan University, Chengdu 610065, China

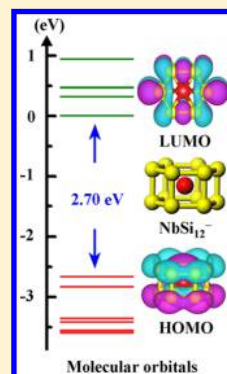
[‡]Department of Physics, Nanyang Normal University, Nanyang 473061, China

[§]Centre for Science at Extreme Conditions and SUPA, School of Physics and Astronomy, The University of Edinburgh, Edinburgh EH9 3JZ, United Kingdom

^{||}Beijing Computational Science Research Center, Beijing 10084, China

Supporting Information

ABSTRACT: We performed systematic structure searches for low energy structures of neutral and singly charged niobium-doped silicon clusters NbSi_n^Q ($n = 2-20$; $Q = 0, \pm 1$) by means of the CALYPSO structure searching method. A large population of low energy clusters is collected from the unbiased structure search. Subsequent geometry optimizations using density-functional theory with the B3LYP exchange-correlation functional are carried out to determine structural patterns and relative stabilities of various low energy candidates for Nb-doped silicon clusters. Based on the calculated binding energies along with measured photoelectron spectroscopy data, we are able to confirm that our lowest energy structures are the true minima. It is shown that the localized position of the Nb impurity atom in $\text{NbSi}_n^{0/\pm 1}$ clusters gradually moves from the convex capping position, to surface-substituted, to the concave, and in the end to the encapsulated state as the number of Si atoms increases from 2 to 20. The lowest energy isomer of both neutral and anionic NbSi_{12} cluster is very stable in a high-symmetry endohedral D_{6h} structure in which the Nb atom is placed at the center of a regular hexagonal prism of Si atoms. This makes it an attractive building block for cluster-assembled materials.



1. INTRODUCTION

Emissions of carbon oxides, particularly carbon dioxide (CO_2), have aroused global attention¹⁻⁸ and have evolved into a pressing environmental challenge to humanity in recent decades.⁴⁻⁸ The most effective way to reduce CO_2 emissions is to increase the operational efficiency and decrease the emission of undesired gases in conventional power plants.⁹ Improvements in heat efficiency can usually be realized by increasing the temperature at which the turbines operate.¹⁰ With this in mind, the development of new refractory materials, more advanced than the conventional materials used in turbines, is crucial. Transition-metal silicides, such as niobium silicide, are attractive candidates for structural applications at ultrahigh temperatures above 1350 °C due to their high melting points, superior strength to density ratio, and excellent oxidation resistance at high temperatures.¹¹⁻¹³ In the past few years, extensive work has been performed on niobium silicides. Studies concentrate on the formation of amorphous niobium silicide and have suggested that nanoclusters play a role in such chemical processes. It is therefore very important to explore the evolution of patterns in the microstructure and the electronic properties of niobium silicide aggregates in the transition from the molecular to the condensed phase.

There have been a number of gas-phase experimental studies on the structural and electronic properties of the NbSi nanoalloy clusters.¹⁴⁻¹⁶ Cations/neutrals/anions of silicon clusters doped with one metal atom ($M = \text{Sc}, \text{Y}, \text{Lu}, \text{Ti}, \text{Zr}, \text{Hf}, \text{V}, \text{Nb}, \text{and Ta}$) were generated by the double-laser vaporization method in a modified cluster source, and their stability was characterized with mass spectroscopy, adsorption reactivity, and photoelectron spectroscopy (PES).¹⁵ Combined anion photoelectron spectroscopy and computational studies on the transition metal–silicon diatomic species ($\text{NbSi}, \text{MoSi}, \text{PdSi}, \text{and WSi}$) showed that the composition of the highest occupied molecular orbitals shift from a majority of transition-metal s - and d -orbital contributions in ZrSi and NbSi to mainly silicon p -orbital contributions for MoSi and PdSi .¹⁶ Despite the enormous progress that has been made, relatively little is known about the evolution of structural and electronic properties on Nb-doped silicon clusters, and theoretical studies on medium-size-range clusters are currently lacking. The main reason may be because the computational methods used for small clusters are not practical for medium-sized clusters.

Received: September 28, 2015

Revised: December 18, 2015

Published: December 21, 2015

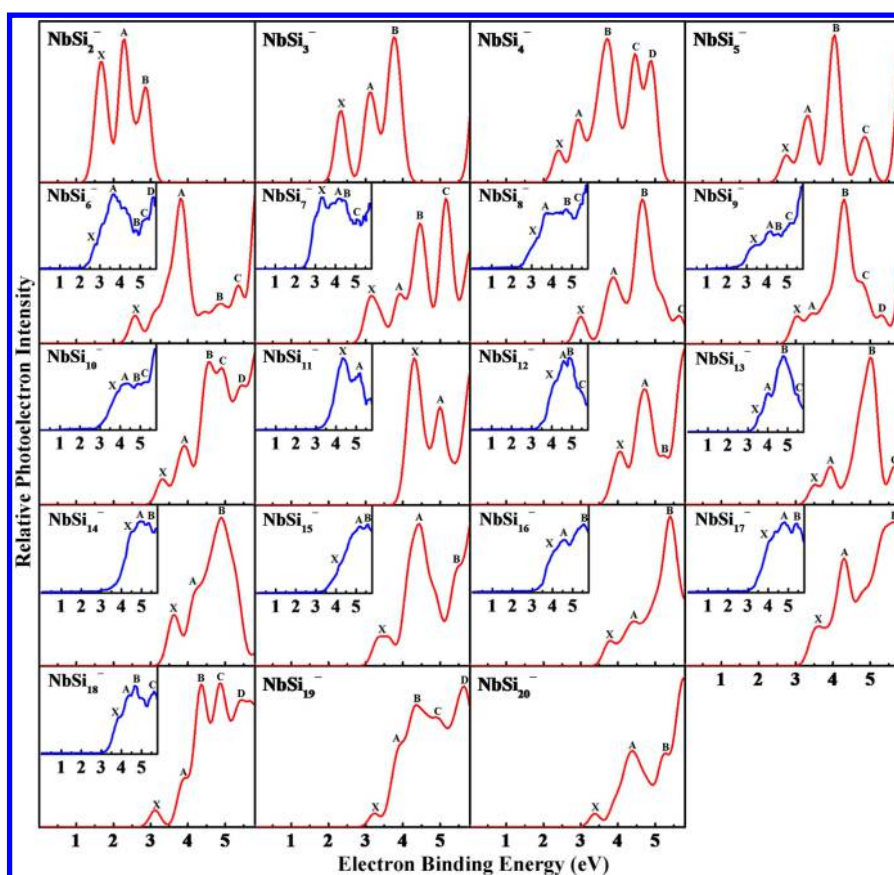


Figure 1. Comparison of the simulated photoelectron spectra with the experimental PES from ref 50 of lowest energy NbSi_n^- ($n = 2-20$) clusters.

Moreover, the determination of the true global minimum structure of a given cluster size is a challenging problem because of the much increased complexity of the potential surface and the exponential increase of the number of low energy structures with cluster size.¹⁷⁻²²

In order to verify existing experimental results and to examine the relative stability of the metal Nb atom encapsulated inside Si clusters, we have carried out extensive structure searches of neutral and charged Nb-doped silicon clusters in the size range from 2 to 20 using the CALYPSO (Crystal structure AnaLYsis by Particle Swarm Optimization) package.²³⁻²⁷ The following interesting results have emerged: (i) When the transition-metal Nb is doped into silicon clusters, the position of the Nb impurity atom gradually moves, with increasing cluster size, from a convex capping site to a surface substitute site, then to a concave, and in the end to an encapsulated site. (ii) While Nb occupies an endohedral position in most neutral and anionic clusters, the structure of NbSi_{12} is highly symmetric, with Nb centered in a Si_{12} hexagonal prism. (iii) The structural properties of Nb-doped silicon clusters are different from those of pure silicon clusters, implying that doping the transition metal Nb atom into pure silicon clusters has significant effects on their stability and electronic properties. The paper is organized as follows. In section 2, we describe the details of the computational method, while in section 3 we present our results and discussion. Finally, we summarize our main conclusions in section 4.

2. COMPUTATIONAL DETAILS

We used the CALYPSO method to search for the geometries of low-lying isomers of neutral and charged Nb-doped silicon

clusters.²³ A local version of the particle swarm optimization (PSO) algorithm is implemented to utilize efficient global minimization of free-energy surfaces for a given nonperiodic system. The algorithm can identify stable structures based on only the chemical composition. It has made a variety of successful predictions for structures of, for example, nanoparticles,²⁴ layered materials,²⁵ crystals,^{26,28} clusters,^{27,29,30} and so on. Details of the theoretical methodology have been published elsewhere. Here, structure predictions of neutral and charged Nb-doped silicon clusters up to 20 silicon atoms are carried out. In the particle swarm optimization method, cluster structures are ordered by generations. Each generation contains 50 structures, 60% of which are generated by the particle swarm optimization algorithm, while the others are generated randomly. We have followed 30 generations to achieve convergence around the lowest minima of the potential energy surface. The searches generated a large database for low energy neutral, anionic and cationic Nb-doped silicon clusters. Low energy structures within 4 eV of the global minimum structure were reoptimized with subsequent frequency calculations. The calculations are performed within the spin unrestricted density functional theory method with the hybrid B3LYP^{31,32} exchange-correlation functional. The LANL2DZ³³ basis set for the transition-metal Nb atom and the 6-311+G(d) basis set for Si atom were used. The effect of the spin multiplicity was considered (up to septet and octet) and no symmetry constraints are enforced during the geometry optimization. For each isomer, harmonic vibrational frequencies are calculated to make sure that the structures correspond to real local minima without imaginary frequency. All calculations are performed using the Gaussian 09 program package.³⁴ The

photoelectron spectra are simulated using the time-dependent-DFT (TD-DFT) method, which provides a first-principal method for the calculation of excitation energies and can be used to calculate the positions of the PES peaks exactly. This approach has applied successfully in recent years to studies of organic molecules and small clusters.^{35–37} Chemical-bonding analysis is performed using the adaptive natural density partitioning (AdNDP)³⁸ method.

The accuracy of the B3LYP functional has been found to be questionable for bulk solids, involving metal atoms.^{39–41} Paier et al.³⁹ concluded that B3LYP gives much larger errors than PBE0,^{42,43} in particular, for transition metals, on lattice constants, bulk modulus, and atomization energies. We have therefore reoptimized all of the low-lying isomers with the PBE0 functional and performed frequency calculations as well. The choice of PBE0 functional is based on some previous reports.^{39,44,45} The structural and energy trends obtained using the PBE0 functional are found to be the same as obtained using the B3LYP functional, with a slight increase in the total energy values in case of the PBE0 functional as compared to the B3LYP functional. The relative energy trends obtained with the PBE0 functional are listed in Table S1 (in the Supporting Information, SI). Compared with the experimental PES of Nb-doped silicon clusters (discussed below), we can also see that the results from the B3LYP level (Figure 1) are better than those from the PBE0 functional (Figure S1) for NbSi_n^- clusters. In fact, B3LYP is the most popular “hybrid” functional in the quantum chemistry community and will allow for reliable comparisons of these results.^{46–48} We believe that the B3LYP exchange-correlation functional can give reliable structures and energies for Nb-doped silicon clusters, and here we base our discussion on B3LYP results.

3. RESULTS AND DISCUSSION

3.1. Geometric Structure. We have performed unbiased searches for the global minima structures of neutral, anionic, and cationic Nb-doped silicon clusters in the size range $2 \leq Q \leq 20$. A large number of isomers, about 1000–1500 isomers, are obtained for each cluster size and optimized during the structure searches. Here, we concentrate on the lowest energy structures and some important structural isomers for the neutral, anionic, and cationic species. The lowest energy structures of neutral, anionic, and cationic NbSi_n^Q ($n = 2–20$; $Q = 0, \pm 1$) clusters are displayed in Figure 2. All structures are confirmed to be energetic minima from analysis of their vibrational frequencies. Most of the optimized structures are found to prefer a low spin state, i.e., the singlet state for closed-shell and the doublet state for open-shell clusters. The electronic states and point group symmetry of all these lowest energy clusters are summarized in Table 1. The harmonic vibrational frequencies are listed in Tables S2–S4 (SI). Other typical low-lying isomers of NbSi_n^Q ($n = 2–20$; $Q = 0, \pm 1$) clusters together with their point groups and relative energies are shown in Figures S2–S4 in the SI.

For both neutral and charged species, only the smallest cluster ($n = 2$) forms planar structures. For $n \geq 3$, it is evident that the equilibrium structures are three-dimensional configurations. In the lowest energy structure of both neutral and charged NbSi_3 clusters, three Si atoms form a regular triangle and the Nb atom joins at the apex to form a trigonal pyramid. The lowest energy geometries of NbSi_4^Q ($Q = 0, \pm 1$) are slightly distorted trigonal bipyramids. The four Si atoms form a folding plane of the trigonal bipyramid, which is capped by the



Figure 2. Lowest energy structures of NbSi_n^Q ($n = 2–20$; $Q = 0, \pm 1$) clusters. The red (yellow) spheres represent the Nb (Si) atoms.

Nb atom. As for the most stable structure of NbSi_5^Q ($Q = 0, \pm 1$) clusters, both C_1 symmetry NbSi_5^Q and C_s symmetry NbSi_5^Q can be viewed as a boat-shaped structure with the doped Nb atoms at different positions. The C_{4v} symmetry NbSi_5^- cluster can be viewed as a Si atom capping the bottom of a distorted NbSi_4^- cluster, forming a square bipyramid. As the number of Si atoms increases, the preferred position of the Nb atom gradually moves from convex capped sites to encapsulated sites. In the $\text{NbSi}_{10,11}^Q$ ($Q = 0, \pm 1$) clusters, the Nb atom tends to move inside a caged silicon framework (except for NbSi_{10}^+ , where the Nb atom still localizes at the surface site of the silicon frame). We find that the Nb atom is fully encapsulated by the silicon framework for $n \geq 12$. From $n = 12$ through $n = 20$, the lowest energy structures of NbSi_n^Q ($Q = 0, \pm 1$) are distorted Si cages surrounding the Nb impurity. In addition, except for NbSi_{17}^- and NbSi_{19}^- , the lowest energy structures of NbSi_n^Q ($n = 17–20$; $Q = 0, \pm 1$) clusters can be seen as double cage structures, where the Nb atom is encapsulated by two connected silicon units. It should be mentioned that the lowest energy isomers of neutral and anionic NbSi_{12}^Q ($Q = 0, -1$) clusters can be found very quickly, typically within 10 generations. For cationic NbSi_{12}^+ , however, the lowest energy structure was much harder to obtain, largely because there are two competing lowest-energy isomers with very different structures. More interestingly, and in contrast to cationic

Table 1. Electronic States, Symmetries, Average Binding Energies E_b (eV), HOMO–LUMO Energy Gaps E_{gap} (eV), and Charge Q (e) on Nb Atom of NbSi_n^Q ($n = 2-20$; $Q = 0, \pm 1$) Clusters

| NbSi_n | | | | | | NbSi_n^- | | | | | | NbSi_n^+ | | | | | |
|-----------------|-------------------|-----------------|-------|------------------|----------------|-------------------|-------------------|-----------------|-------|------------------|----------------|-------------------|----------------|-----------------|-------|------------------|----------------|
| n | sta | sym | E_b | E_{gap} | $Q(\text{Nb})$ | n | sta | sym | E_b | E_{gap} | $Q(\text{Nb})$ | n | sta | sym | E_b | E_{gap} | $Q(\text{Nb})$ |
| 2 | $^2\text{B}_2$ | C_{2v} | 1.99 | 0.53 | 0.04 | 2 | $^1\text{A}_1$ | C_{2v} | 2.66 | 1.68 | -0.55 | 2 | $^1\text{A}_1$ | C_{2v} | 2.10 | 1.49 | 0.44 |
| 3 | $^2\text{A}'$ | C_s | 2.77 | 2.00 | -0.11 | 3 | $^1\text{A}_1$ | C_{3v} | 3.21 | 2.43 | -0.80 | 3 | $^3\text{A}_1$ | C_{3v} | 2.68 | 2.26 | -0.17 |
| 4 | $^4\text{B}_1$ | C_{2v} | 2.74 | 1.22 | 0.09 | 4 | $^1\text{A}'$ | C_s | 3.27 | 2.09 | -0.75 | 4 | $^1\text{A}_1$ | C_{3v} | 2.97 | 2.97 | -0.04 |
| 5 | ^2A | C_1 | 3.00 | 1.81 | -0.53 | 5 | $^1\text{A}_1$ | C_{4v} | 3.41 | 2.39 | -0.91 | 5 | $^3\text{A}''$ | C_s | 3.00 | 1.63 | 0.11 |
| 6 | ^2A | C_1 | 3.11 | 1.92 | -0.57 | 6 | ^1A | C_1 | 3.35 | 1.85 | -0.84 | 6 | $^1\text{A}'$ | C_s | 3.19 | 2.64 | -0.58 |
| 7 | $^2\text{A}'$ | C_s | 3.20 | 1.56 | -0.91 | 7 | $^1\text{A}'$ | C_s | 3.51 | 2.31 | -1.08 | 7 | ^1A | C_1 | 3.21 | 2.53 | -0.59 |
| 8 | ^4A | C_1 | 3.11 | 0.90 | -0.79 | 8 | $^1\text{A}_1$ | C_{2v} | 3.50 | 2.04 | -1.59 | 8 | ^1A | C_1 | 3.27 | 2.00 | -0.89 |
| 9 | ^2A | C_1 | 3.21 | 1.40 | -1.67 | 9 | ^1A | C_1 | 3.46 | 2.04 | -1.54 | 9 | ^1A | C_1 | 3.28 | 2.15 | -1.33 |
| 10 | ^2A | C_1 | 3.23 | 1.26 | -1.77 | 10 | $^1\text{A}'$ | C_s | 3.51 | 1.95 | -2.33 | 10 | ^1A | C_1 | 3.26 | 2.36 | -0.93 |
| 11 | ^2A | C_1 | 3.28 | 1.51 | -2.56 | 11 | $^1\text{A}_1$ | C_{2v} | 3.54 | 2.76 | -3.42 | 11 | $^1\text{A}_1$ | C_{2v} | 3.32 | 1.89 | -2.26 |
| 12 | $^2\text{B}_{2u}$ | D_{6h} | 3.37 | 1.03 | -3.40 | 12 | $^1\text{A}_{1g}$ | D_{6h} | 3.63 | 2.70 | -3.55 | 12 | ^1A | C_1 | 3.34 | 1.95 | -2.97 |
| 13 | ^2A | C_1 | 3.32 | 1.29 | -3.78 | 13 | ^1A | C_1 | 3.61 | 2.11 | -3.48 | 13 | ^1A | C_1 | 3.37 | 1.85 | -2.88 |
| 14 | ^4A | C_1 | 3.41 | 1.27 | -3.61 | 14 | $^3\text{A}''$ | C_s | 3.60 | 1.22 | -3.59 | 14 | ^1A | C_1 | 3.43 | 1.59 | -3.74 |
| 15 | $^2\text{A}'$ | C_s | 3.40 | 1.19 | -4.36 | 15 | ^1A | C_1 | 3.52 | 1.57 | -3.72 | 15 | ^3A | C_1 | 3.44 | 1.27 | -3.78 |
| 16 | $^2\text{B}_1$ | C_{2v} | 3.50 | 1.16 | -3.52 | 16 | ^1A | C_1 | 3.66 | 1.90 | -3.63 | 16 | $^1\text{A}_1$ | D_{4h} | 3.56 | 2.44 | -3.63 |
| 17 | ^2A | C_1 | 3.39 | 1.16 | -3.65 | 17 | ^1A | C_1 | 3.55 | 1.67 | -3.52 | 17 | ^1A | C_1 | 3.40 | 1.85 | -3.10 |
| 18 | ^4A | C_1 | 3.36 | 0.79 | -3.30 | 18 | ^1A | C_1 | 3.53 | 1.38 | -3.51 | 18 | ^1A | C_1 | 3.44 | 1.81 | -3.79 |
| 19 | ^2A | C_1 | 3.39 | 1.10 | -3.06 | 19 | ^3A | C_1 | 3.55 | 0.76 | -3.43 | 19 | ^1A | C_1 | 3.45 | 1.55 | -3.69 |
| 20 | ^2A | C_1 | 3.40 | 1.01 | -3.73 | 20 | ^1A | C_1 | 3.53 | 1.26 | -3.50 | 20 | ^1A | C_1 | 3.44 | 1.63 | -3.74 |

NbSi_{12}^+ , the equilibrium geometries of neutral NbSi_{12} and anionic NbSi_{12}^- cluster are the most symmetric with a hexagonal biprism Si cage geometry. Within, the Nb atom is sandwiched between two hexagonal planes of Si atoms. This structure is analogous to the metal-bis benzene complex, where the metal atom is sandwiched between two benzene molecules with a D_{6h} geometry.⁴⁹

3.2. Photoelectron Spectra of Anionic NbSi_n^- Clusters.

To probe whether the geometries, as shown in Figure 2, are indeed the ground-state structures of NbSi_n^Q ($n = 2-20$; $Q = 0, \pm 1$) clusters, the photoelectron spectra of anionic NbSi_n^- ($n = 2-20$) clusters are simulated using TD-DFT and compared to the available experimental results.⁵⁰ The simulated spectra of ground state structures combine with the experimental PES are displayed in Figure 1. The simulated spectra of other low energy isomers are shown in Figure S1. Each peak of the PES represents a transition from the ground state of the cluster anion to the ground or an excited state of their corresponding neutrals. The simulated spectrum of NbSi_2^- shows three major peaks (X, A, and B) and the first peak (X) is located around 1.65 eV, which gives the vertical detachment energy (VDE). The VDE of NbSi_3^- is about 2.33 eV. After the first peak, there are two peaks between 3 and 4 eV. The first three peaks (X, A, and B) of the PES of NbSi_4^- are similar to those of NbSi_3^- and the VDE is about 2.40 eV. For NbSi_5^- , there are four major peaks and the first peak (X) is very small, corresponding to a VDE of 2.74 eV. The simulated spectrum of NbSi_6^- exhibits a weak peak (X) centered at 2.58 eV and an intense peak (A) at 3.80 eV, which successfully reproduces the experimental features. The calculated VDE is also in good agreement with the experimental result of 2.75 eV. For NbSi_7^- , four discrete peaks (X, A–C) are found at 3.15, 3.90, 4.45, and 5.15 eV in the simulated spectrum. A similar four-peak structure is also seen in the experimental PES and the VDE is in agreement with experimental value 3.29 eV. For the PES of NbSi_8^- , both theoretical and experimental measurements yield four peaks (X, A–C) and have similar VDE value. For NbSi_9^- , the four

obvious peaks (A–D) seen in the simulated PES are in general agreement with the experimental spectrum, while the first peak (X) is at unexpectedly low energy, at 3.02 eV. Similar situations occur for both NbSi_{10}^- and NbSi_{18}^- , namely, there is an excess peak (X) obtained in the simulated PES. The simulated spectrum of NbSi_{11}^- yields two obvious peaks (X and A) at 4.26 and 5.00 eV, in very good agreement with the experimental results. The simulated PES of NbSi_{12}^- exhibits a small broadened feature, and the first small peak appears at 4.05 eV, which is very close to the experimental result. For NbSi_{13}^- , the simulated spectrum agrees excellently with experiment and contains four peaks (X, A–C). In the simulated spectrum of NbSi_{14}^- , three peaks are observed as in the experimental PES, although the overall spectrum is slightly broader and moved to lower energy compared to experiment. A similar situation occurs for NbSi_{15}^- . For NbSi_{16}^- , the experimental spectrum is successfully reproduced by the simulated spectrum, both of them shows the same trend and yield three peaks (X, A, and B). In the PES of NbSi_{17}^- , three peaks (X, A, and B), which increase in height, can be seen in both experimental and theoretical results. The simulated spectrum of NbSi_{19}^- shows four almost evenly spaced obvious peaks (A–D) and one weak peak (X), in which the VDE is about 3.23 eV. For NbSi_{20}^- , the simulated spectrum yields three peaks (X, A and B) at 3.38, 4.40, and 5.25 eV, respectively. As stated above, we find that the simulated PES spectra of anionic NbSi_n^- ($n = 2-20$) clusters are mostly in very good agreement with experiments, confirming that the ground-state structures we obtained are true global minima.

3.3. Ionization Potential, Electron Affinity, and Charge Transfer. The calculated adiabatic ionization potential (AIP), vertical ionization potential (VIP), vertical electronic affinity (VEA), adiabatic electronic affinity (AEA), and VDE of niobium-doped silicon clusters are summarized in Table 2, together with the available experimental data for comparison. The ionization potential and electron affinity potential as functions of cluster size are shown in Figure 3. From Figure 3a,

Table 2. Calculated VIP, AIP, VEA, AEA, and VDE Values for the Lowest Energy NbSi_n^Q ($n = 2-20$; $Q = 0, \pm 1$) Clusters together with the Available Experimental Data for Comparison (All Energies in eV)

| <i>n</i> | NbSi_n | | | NbSi_n^- | | | |
|----------|-----------------|-------|-------|-------------------|-------------------|-------|-------------------|
| | VIP | VEA | AIP | AEA | | VDE | |
| | calcd | calcd | calcd | calcd | expt ^a | calcd | expt ^a |
| 2 | 5.99 | 2.81 | 6.53 | 2.48 | | 1.65 | |
| 3 | 7.64 | 2.23 | 7.20 | 2.23 | | 2.33 | |
| 4 | 6.65 | 2.41 | 5.76 | 3.09 | | 2.40 | |
| 5 | 7.28 | 2.39 | 6.88 | 2.88 | | 2.74 | |
| 6 | 6.65 | 1.74 | 6.32 | 2.11 | 2.26 | 2.58 | 2.75 |
| 7 | 7.14 | 2.70 | 6.84 | 2.94 | 2.51 | 3.15 | 3.29 |
| 8 | 6.12 | 2.91 | 5.45 | 4.01 | 2.49 | 3.00 | 3.30 |
| 9 | 6.35 | 2.24 | 6.19 | 3.02 | 2.48 | 3.02 | 3.20 |
| 10 | 7.00 | 3.11 | 6.52 | 3.49 | 2.92 | 3.31 | 3.85 |
| 11 | 7.41 | 3.33 | 6.42 | 3.54 | 3.49 | 4.26 | 4.32 |
| 12 | 7.43 | 3.82 | 7.26 | 3.85 | 3.47 | 4.05 | 4.14 |
| 13 | 7.18 | 3.30 | 6.17 | 4.50 | 3.35 | 3.50 | 3.50 |
| 14 | 6.85 | 3.06 | 6.50 | 3.38 | 3.31 | 3.66 | 4.00 |
| 15 | 6.47 | 2.86 | 6.35 | 2.30 | 3.28 | 3.32 | 4.04 |
| 16 | 6.01 | 2.40 | 5.80 | 3.31 | 3.07 | 3.80 | 4.06 |
| 17 | 6.75 | 3.30 | 6.68 | 3.37 | 3.06 | 3.60 | 4.03 |
| 18 | 6.10 | 3.00 | 5.39 | 3.65 | 3.29 | 3.12 | 3.82 |
| 19 | 6.25 | 2.91 | 5.69 | 3.61 | | 3.23 | |
| 20 | 6.33 | 3.13 | 6.13 | 3.24 | | 3.38 | |

^aReference 50.

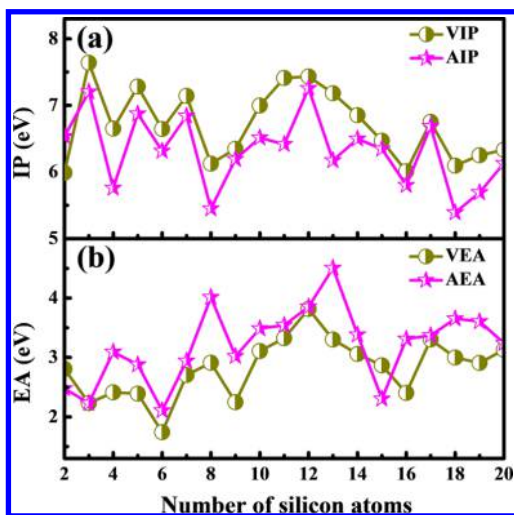


Figure 3. Ionization potential (a) and electron affinity (b) of NbSi_n^Q ($n = 2-20$; $Q = 0, \pm 1$) clusters.

the same oscillation of IP curves for AIP and VIP is present except for $n = 11$ and 13 . It means that obvious geometric rearrangements appear in the corresponding geometry with removal of an electron from the neutral $\text{NbSi}_{11,13}$ clusters (see Figure 2). As shown in Figure 3b, the EA curves of AEA and VEA show similar oscillations in the region of $n = 2-12$ while sporting different trends for $n = 13-20$. The deviation may be explained by diversity between the lowest energy structure of neutral and anionic clusters. It should be noted that the difference between AEA and VEA of $n = 3, 12$, and 17 is about 0.00, 0.03, and 0.07 eV, indicating that the anionic $\text{NbSi}_{3,12,17}^-$ cluster basically keeps the structural framework of the corresponding neutral state.

The charge on Nb atom for the lowest energy NbSi_n^Q ($n = 2-20$; $Q = 0, \pm 1$) clusters by natural population analysis (NPA) is shown in Table 1. Except for NbSi_2 and NbSi_4 , it is found that the charge of Nb atom is negative for all the neutral species, which means that, in most of the cases, the Si atoms act as a donor and the Nb atom is an acceptor. For cluster size of $n = 5-20$, the transfer negative charges increase significantly and reaches a maximum value of $-4.36e$ at $n = 15$. In the case of anions, the extra electron is located on both the Nb atom and the Si_n framework with $n = 2-6$ because the charge on Nb atom is smaller than 1 ($-e$). For the anions with $n \geq 7$, the charge on Nb atom is larger than the extra electron. In other words, there is electron transfer from the Si_n framework to the Nb atom. The largest charge on Nb atom is $-3.72e$ occurred on NbSi_{15}^- . The charges on the Nb atom of cationic clusters show that the extra positive charge is mainly donated from Si_n framework. The natural electron configuration (NEC) for the lowest energy NbSi_n^Q ($n = 2-20$; $Q = 0, \pm 1$) clusters are listed in Tables S5–S7 (SI). Quite clearly, the charges transfer from Si atoms to the Nb atom, which is consistent to the above NPA analysis. Except for a few structures like NbSi_{15} , the deviation of natural charges on Nb atoms in NbSi_n^Q ($n = 2-20$; $Q = 0, \pm 1$) is less than $1e$ during the structure transformation of forming a cage-like structure, especially for the anionic clusters.

3.4. Relative Stabilities and HOMO–LUMO Gaps. The average binding energy (E_b) of a cluster is a useful measure of its inherent stability and is defined as follows

$$E_b = \frac{nE(\text{Si}) + E(\text{Nb}^Q) - E(\text{NbSi}_n^Q)}{n + 1}, \quad Q = 0, \pm 1 \quad (1)$$

where E is the total energy of the corresponding cluster or atom. The E_b of ground state NbSi_n^Q ($n = 2-20$; $Q = 0, \pm 1$) clusters as a function of the number n of Si atoms are plotted in Figure 4a. Larger E_b values indicate higher stability. Except for NbSi_3 and NbSi_{12} , all of the neutral NbSi_n have lower E_b values than their cationic and anionic states, suggesting that it is generally energetically favorable for the neutral NbSi_n species either to donate or receive charge. It is also easily seen that for all three charge states of the clusters, the binding energies gradually increase with growing cluster size and feature a distinct maximum at $n = 16$, signifying that $\text{NbSi}_{16}^{0/+}$ are the most stable clusters in the range studied here. For larger clusters, $n > 16$, the binding energies decrease somewhat. For the neutral and anionic species, two additional local maxima of the binding energy are found $n = 7$ and 12 , indicating that these cluster sizes are more stable than their adjacent sized clusters. For the cationic clusters, three slight local maxima of E_b show that $\text{NbSi}_{4,6,8}^+$ have relatively strong energetic stability.

The second-order difference of the energy (Δ^2E) can reflect the relative stability of neutral and charged clusters compared to their smaller or larger neighbors. For NbSi_n^Q ($n = 2-20$; $Q = 0, \pm 1$) clusters, Δ^2E can be defined as

$$\Delta^2E = E(\text{NbSi}_{n-1}^Q) + E(\text{NbSi}_{n+1}^Q) - 2E(\text{NbSi}_n^Q), \quad Q = 0, \pm 1 \quad (2)$$

The Δ^2E values for all NbSi_n^Q ($n = 2-20$; $Q = 0, \pm 1$) clusters are shown in Figure 4b. It shows similar odd–even oscillating behaviors in the range of $n = 2-8$ and $n = 11-19$ for neutrals and anions. Several distinct peaks are found at $n = 3, 5, 7, 12, 14$, and 16 , indicating that the clusters $\text{NbSi}_3^{0/-}$, $\text{NbSi}_5^{0/-}$, $\text{NbSi}_7^{0/-}$, $\text{NbSi}_{12}^{0/-}$, $\text{NbSi}_{14}^{0/-}$, and $\text{NbSi}_{16}^{0/-}$ are more stable

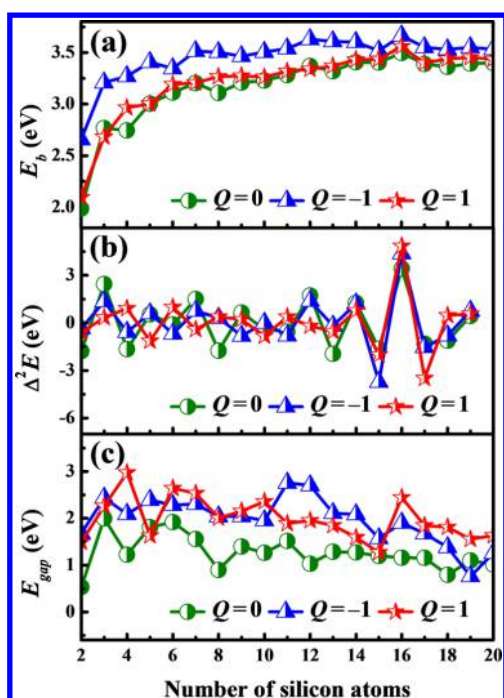


Figure 4. Size dependence of (a) the averaged binding energies E_b , (b) second-order energy differences $\Delta^2 E$, and (c) HOMO–LUMO energy gaps E_{gap} for NbSi_n^Q ($n = 2\text{--}20$; $Q = 0, \pm 1$) clusters.

than their neighbors. This result is in accordance with the findings from the average binding energy. For cationic NbSi_n^+ clusters, an irregular oscillating behavior occurs in the range of $n < 13$, and an odd–even oscillation, which is similar to the neutral species, is also found for the cations with $n = 13\text{--}18$.

The HOMO–LUMO energy gap (E_{gap}) is a useful quantity to represent the ability of an electron to jump from occupied orbitals to unoccupied orbitals. Larger values of E_{gap} represent stronger chemical stability. The evolution of HOMO–LUMO energy gaps E_{gap} for the ground-state NbSi_n^Q ($n = 2\text{--}20$; $Q = 0, \pm 1$) clusters are shown in Figure 4c. Comparing the E_{gap} of the clusters in all three charge states, it can be seen clearly that, except for NbSi_5^+ and NbSi_{19}^- , the E_{gap} of both anions and cations are higher than the corresponding neutral state. This suggests neutral clusters are less stable, which is in excellent agreement with the results of averaged binding energies shown in the Figure 4a. As for anionic NbSi_n^- clusters, three local maxima for E_{gap} values of 2.76 eV, 2.70, and 1.90 eV are found at $n = 11$, 12, and 16, respectively, suggesting that $\text{NbSi}_{11,12,16}^-$ are more stable than other clusters. The local maxima of the E_{gap} for neutral and cationic clusters suggest that neutral $\text{NbSi}_{3,6,9,11}$ and cationic $\text{NbSi}_{4,6,10,16}^+$ possess enhanced relative stability. Combining the above analysis on E_b , $\Delta^2 E$, and E_{gap} values of NbSi_n^Q ($n = 2\text{--}20$; $Q = 0, \pm 1$) clusters, the cationic NbSi_{16}^+ as well as anionic $\text{NbSi}_{7,12,16}^-$ can be viewed as “magic” clusters with enhanced stability.

3.5. Chemical-Bonding Analysis. For an in-depth understanding of the bonding nature of the niobium-doped silicon clusters, we analyzed their molecular orbitals (MOs). For simplicity, we present here only the molecular orbitals along with the energy levels of the NbSi_{12}^- cluster, which features one of the largest HOMO–LUMO energy gaps, 2.70 eV, across all clusters studied (see Figure 5). The LUMO, corresponding to Si–Si σ bonds, is formed primarily by s - and p -orbitals of peripheral Si atoms. For the occupied MOs HOMO, HOMO-5,

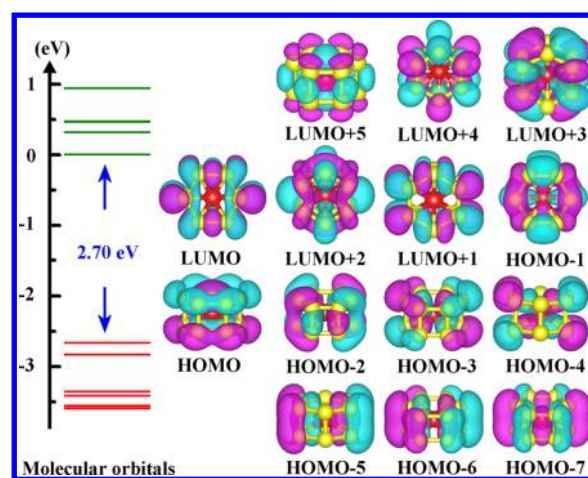


Figure 5. Molecular orbitals and energy levels of anionic NbSi_{12}^- cluster. The HOMO–LUMO gap is indicated (in blue).

HOMO-6, and HOMO-7, the combination of p -orbitals in the peripheral Si atoms results predominantly in the formation of delocalized π bonds. The HOMO-1 features σ bonds between the p -orbitals of the peripheral Si atoms and the d -orbital of the central Nb atom, and the MOs HOMO-2, HOMO-3, and HOMO-4 form $\sigma + \pi$ hybrid orbitals through mixing of Si p -orbitals with the Nb d -orbital. These molecular orbitals illustrate that there are strong interactions between the central Nb and the cage Si atoms. The pd hybridization between the Si and Nb atom interactions strengthens the Si–Nb bonds and, therefore, makes the high-symmetry endohedral D_{6h} structure of NbSi_{12}^- more stable. Meanwhile, the occupation of the d -orbital may cause the Nb atom to be negatively charged and stabilize the Nb atom encapsulated within the silicon cage.

The AdNDP method is an efficient tool to decipher the chemical bonding of clusters. As an extension of the MO analysis, AdNDP represents the bonding of a molecule in terms of n -center two-electron ($nc\text{--}2e$) bonds, which including the localized ($1c\text{--}2e$ lone pairs and $2c\text{--}2e$ bonds) and delocalized ($nc\text{--}2e$ bonds, $3 \leq n \leq$ total number of atoms in the system). Figure 6 depicts the AdNDP bonding pattern for the NbSi_{12}^- cluster. The AdNDP analysis reveals 12 localized bonds and 16 delocalized bonds with occupation numbers (ONs) ranging from 1.78 to 2.00 lel. The peripheral Si–Si bonds include localized bonding in the form of six $2c\text{--}2e$ σ bonds with an occupation number of ON = 1.95 lel and six $2c\text{--}2e$ σ bonds with an occupation number of ON = 1.83 lel. For these bonds, each Si atom in NbSi_{12}^- can be considered as contributing one σ electron to a $2c\text{--}2e$ σ bond along one Si_2 unit. The delocalized bonding consists of six $3c\text{--}2e$ σ bonds (ON = 1.90 lel), six $3c\text{--}2e$ π bonds (ON = 1.78 lel), three $9c\text{--}2e$ π bonds (ON = 1.93 lel) and one $12c\text{--}2e$ σ bonds with ON = 2.00 lel. Each pair of individual Si_2 units can be viewed as contributing one σ electron to form a $3c\text{--}2e$ σ bond with the central Nb atom, while there is also a delocalized $3c\text{--}2e$ π bond between Si_2 units and Nb atom in the NbSi_{12}^- cluster. We think that the balance between $3c\text{--}2e$ π and $3c\text{--}2e$ σ bonding pattern in NbSi_{12}^- contributes to their large HOMO–LUMO gap (2.70 eV). The $9c\text{--}2e$ bonds describe three completely delocalized π bonds with 6 electrons, and embody the strong bond between the $4d$ -orbital of Nb and the peripheral Si_{12} cage. For the $12c\text{--}2e$ σ bond, the high occupation number of 2.00 lel may point to its high electronic stability. The availability of p - and d -orbitals in Nb that can participate in the delocalized bonding with the

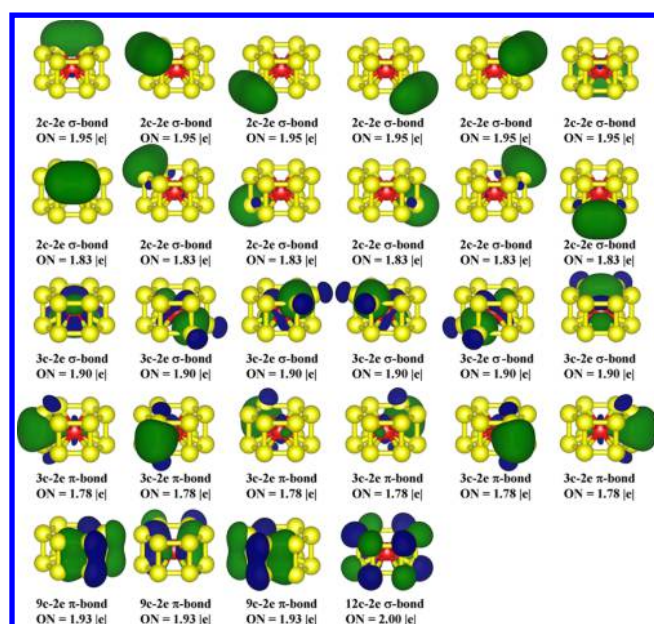


Figure 6. AdNDP chemical bonding analysis of the NbSi_{12}^- cluster. ON denotes the occupation number and is equal to 2.00 |e| in the ideal case.

peripheral Si atoms leads to substantial stabilization of the D_{6h} symmetry structure of NbSi_{12}^- and makes it the global minimum structure.

4. CONCLUSIONS

In summary, we have performed a global minimum search for the lowest-energy structures of neutral and charged NbSi_n^Q ($n = 2-20$; $Q = 0, \pm 1$) clusters by using the unbiased CALYPSO method combined with density functional theory geometry optimization. Accurate ab initio methods are used to determine relative stabilities and energy ranking among candidates of low-lying isomers. The optimized geometries of the Nb-doped silicon clusters reveal that the metal Nb atom moves gradually from convex capped to surface substituted, to concave, and to encapsulated sites with increasing size of the silicon clusters, and the formation of endohedral structures strongly depends on the size of the cluster. In particular, neutral and anionic NbSi_{12} clusters are found to be regular hexagonal prisms with the Nb atom at the center. The simulated photoelectron spectroscopy is in good agreement with the experimental data across the range of cluster sizes studies. This result further gives us strong confidence to confirm that the lowest energy structures of the NbSi_n clusters are truly global minimum. We hope that these findings will further stimulate research on transition-metal encapsulated Si-based clusters or other semiconductor clusters.

■ ASSOCIATED CONTENT

Supporting Information

The Supporting Information is available free of charge on the ACS Publications website at DOI: 10.1021/acs.jpcc.5b09453.

Low-lying isomers, vibrational frequencies, and natural electron configuration of neutral and charged niobium-doped silicon clusters NbSi_n^Q ($n = 2-20$; $Q = 0, \pm 1$) (PDF)

■ AUTHOR INFORMATION

Corresponding Authors

*Tel: +86-28-85403803. E-mail: scu_kuang@163.com.

*Tel: +86-377-63513721. E-mail: lucheng@calypso.cn.

Notes

The authors declare no competing financial interest.

■ ACKNOWLEDGMENTS

This work was supported by the National Natural Science Foundation of China (Nos. 11274235 and 11304167), Program for Science & Technology Innovation Talents in Universities of Henan Province (No. 15HASTIT020), Open Project of State Key Laboratory of Superhard Materials (No. 201405), and 973 Program of China (2014CB660804).

■ REFERENCES

- (1) Raymond, P.; Hartmann, J.; Lauerwald, R.; Sobek, S.; McDonald, C.; Hoover, M.; Butman, D.; Strieg, R.; Mayorga, E.; Humborg, C.; Kortelainen, P.; Dürr, H.; Meybeck, M.; Ciais, P.; Guth, P. Global Carbon Dioxide Emissions from Inland Waters. *Nature* **2013**, *503*, 355–359.
- (2) Yin, W.; Krack, M.; Wen, B.; Ma, S.; Liu, L. CO₂ Capture and Conversion on Rutile TiO₂ (110) in the Water Environment: Insight by First-Principles Calculations. *J. Phys. Chem. Lett.* **2015**, *6*, 2538–2545.
- (3) Xiang, Z.; Leng, S.; Cao, D. Functional Group Modification of Metal-Organic Frameworks for CO₂ Capture. *J. Phys. Chem. C* **2012**, *116*, 10573–10579.
- (4) Gattuso, J.; Magnan, A.; Billé, R.; Cheung, W.; Howes, E.; Joos, F.; Allemand, D.; Bopp, L.; Cooley, S.; Eakin, C.; et al. Contrasting Futures for Ocean and Society from Different Anthropogenic CO₂ Emissions Scenarios. *Science* **2015**, *349*, 45–55.
- (5) Brennecke, J.; Gurkan, B. Ionic Liquids for CO₂ Capture and Emission Reduction. *J. Phys. Chem. Lett.* **2010**, *1*, 3459–3464.
- (6) Davis, S.; Caldeira, K.; Matthews, H. Future CO₂ Emissions and Climate Change from Existing Energy Infrastructure. *Science* **2010**, *329*, 1330–1333.
- (7) Licht, S.; Wu, H. STEP Iron, a Chemistry of Iron Formation without CO₂ Emission: Molten Carbonate Solubility and Electrochemistry of Iron Ore Impurities. *J. Phys. Chem. C* **2011**, *115*, 25138–25147.
- (8) Olah, G.; Prakash, G.; Goepfert, A. Anthropogenic Chemical Carbon Cycle for a Sustainable Future. *J. Am. Chem. Soc.* **2011**, *133*, 12881–12898.
- (9) Aizenstat, Z.; Green, U.; Stark, S.; Weidner, C.; Cohen, H. Modes of Formation of Carbon Oxides (CO_x ($x = 1, 2$)) From Coals During Atmospheric Storage: Part I Effect of Coal Rank. *Energy Fuels* **2010**, *24*, 6366–6374.
- (10) Robinson, D.; Groll, E. Efficiencies of Transcritical CO₂ Cycles with and without an Expansion Turbine. *Int. J. Refrig.* **1998**, *21*, 577–589.
- (11) van der Linden, M.; Conchúir, B.; Spigone, E.; Niranjan, A.; Zaccone, A.; Cicuta, P. Microscopic Origin of the Hofmeister Effect in Gelation Kinetics of Colloidal Silica. *J. Phys. Chem. Lett.* **2015**, *6*, 2881–2887.
- (12) Schwarz, U.; Wosylus, A.; Rosner, H.; Schnelle, W.; Ormeci, A.; Meier, K.; Baranov, A.; Nicklas, M.; Leipe, S.; Müller, C.; Grin, Y. Dumbbells of Five-Connected Silicon Atoms and Superconductivity in the Binary Silicides MSi₃ (M = Ca, Y, Lu). *J. Am. Chem. Soc.* **2012**, *134*, 13558–13561.
- (13) Chen, S.; Liu, Y.; Fu, H.; He, Y.; Li, C.; Huang, W.; Jiang, Z.; Wu, G. Unravelling the Role of the Compressed Gas on Melting Point of Liquid Confined in Nanospace. *J. Phys. Chem. Lett.* **2012**, *3*, 1052–1055.
- (14) Uchida, N.; Miyazaki, T.; Matsushita, Y.; Sameshima, K.; Kanayama, T. New Semiconducting Silicides Assembled from

Transition-Metal-Encapsulating Si Clusters. *Thin Solid Films* **2011**, *519*, 8456–8460.

(15) Koyasu, K.; Atobe, J.; Akutsu, M.; Mitsui, M.; Nakajima, A. Electronic and Geometric Stabilities of Clusters with Transition Metal Encapsulated by Silicon. *J. Phys. Chem. A* **2007**, *111*, 42–49.

(16) Gunaratne, K.; Berkdemir, C.; Harmon, C.; Castleman, A. Probing the Valence Orbitals of Transition Metal-Silicon Diatomic Anions: ZrSi, NbSi, MoSi, PdSi and WSi. *Phys. Chem. Chem. Phys.* **2013**, *15*, 6068–6079.

(17) Yoo, S.; Zeng, X. Structures and Relative Stability of Medium-Sized Silicon Clusters. IV. Motif Based Low-Lying Clusters Si₂₁-Si₃₀. *J. Chem. Phys.* **2006**, *124*, 054304.

(18) Khanna, S.; Rao, B.; Jena, P. Magic Numbers in Metallo-Inorganic Clusters: Chromium Encapsulated in Silicon Cages. *Phys. Rev. Lett.* **2002**, *89*, 016803.

(19) Zhu, X.; Zeng, X. Structures and Stabilities of Small Silicon Clusters: Ab initio Molecular-Orbital Calculations of Si₇-Si₁₁. *J. Chem. Phys.* **2003**, *118*, 3558–3570.

(20) Zhu, X.; Zeng, X.; Lei, Y. Structures and Stability of Medium Silicon Clusters. II. Ab initio Molecular Orbital Calculations of Si₁₂-Si₂₀. *J. Chem. Phys.* **2004**, *120*, 8985–8995.

(21) Yoo, S.; Zhao, J.; Wang, J.; Zeng, X. Endohedral Silicon Fullerenes Si_N (27 ≤ N ≤ 39). *J. Am. Chem. Soc.* **2004**, *126*, 13845–13849.

(22) Yoo, S.; Zeng, X.; Zhu, X.; Bai, J. Possible Lowest-Energy Geometry of Silicon Clusters Si₂1 and Si₂5. *J. Am. Chem. Soc.* **2003**, *125*, 13318–13319.

(23) Wang, Y.; Lv, J.; Zhu, L.; Ma, Y. CALYPSO: A Method for Crystal Structure Prediction. *Comput. Phys. Commun.* **2012**, *183*, 2063–2070.

(24) Lu, S.; Wang, Y.; Liu, H.; Miao, M.; Ma, Y. Self-Assembled Ultrathin Nanotubes on Diamond (100) Surface. *Nat. Commun.* **2014**, *5*, 3666.

(25) Wang, Y.; Miao, M.; Lv, J.; Zhu, L.; Yin, K.; Liu, H.; Ma, Y. An Effective Structure Prediction Method for Layered Materials Based on 2D Particle Swarm Optimization Algorithm. *J. Chem. Phys.* **2012**, *137*, 224108.

(26) Wang, Y.; Lv, J.; Zhu, L.; Ma, Y. Crystal Structure Prediction via Particle-Swarm Optimization. *Phys. Rev. B: Condens. Matter Mater. Phys.* **2010**, *82*, 094116.

(27) Lv, J.; Wang, Y.; Zhu, L.; Ma, Y. Particle-Swarm Structure Prediction on Clusters. *J. Chem. Phys.* **2012**, *137*, 084104.

(28) Wang, Y.; Ma, Y. Perspective: Crystal Structure Prediction at High Pressures. *J. Chem. Phys.* **2014**, *140*, 040901.

(29) Zhu, L.; Liu, H.; Pickard, C.; Zou, G.; Ma, Y. Reactions of Xenon with Iron and Nickel are Predicted in the Earth's Inner Core. *Nat. Chem.* **2014**, *6*, 645–649.

(30) Lv, J.; Wang, Y.; Zhu, L.; Ma, Y. Predicted Novel High-Pressure Phases of Lithium. *Phys. Rev. Lett.* **2011**, *106*, 015503.

(31) Becke, A. Density Functional Thermochemistry. III. The Role of Exact Exchange. *J. Chem. Phys.* **1993**, *98*, 5648–5652.

(32) Lee, C.; Yang, W.; Parr, R. Development of the Colic-Salvetti Correlation-Energy Formula into a Functional of the Electron Density. *Phys. Rev. B: Condens. Matter Mater. Phys.* **1988**, *37*, 785–789.

(33) Hay, P.; Wadt, W. Ab Initio Effective Core Potentials for Molecular Calculations. Potentials for K to Au Including the Outermost Core Orbitals. *J. Chem. Phys.* **1985**, *82*, 299–310.

(34) Frisch, M.; Trucks, G.; Schlegel, H.; Scuseria, G.; Robb, M.; Cheeseman, J.; Montgomery, J., Jr.; Vreven, T.; Kudin, K.; Burant, J. et al. *Gaussian 09*; Gaussian, Inc.: Wallingford, CT, 2009.

(35) Mundt, M.; Kümmel, S. Photoelectron Spectra of Anionic Sodium Clusters from Time-Dependent Density-Functional Theory in Real Time. *Phys. Rev. B: Condens. Matter Mater. Phys.* **2007**, *76*, 035413.

(36) Chrostowska, A.; Xu, S.; Maziere, A.; Boknevtz, K.; Li, B.; Abbey, E.; Dargelos, A.; Graciaa, A.; Liu, S. UV-Photoelectron Spectroscopy of BN Indoles: Experimental and Computational Electronic Structure Analysis. *J. Am. Chem. Soc.* **2014**, *136*, 11813–11820.

(37) Piazza, Z.; Hu, H.; Li, W.; Zhao, Y.; Li, J.; Wang, L. Planar Hexagonal B₃6 as a Potential Basis for Extended Single-Atom Layer Boron Sheets. *Nat. Commun.* **2014**, *5*, 3113.

(38) Zubarev, D.; Boldyrev, A. Developing Paradigms of Chemical Bonding: Adaptive Natural Density Partitioning. *Phys. Chem. Chem. Phys.* **2008**, *10*, 5207–5217.

(39) Paier, J.; Marsman, M.; Kresse, G. Why Does the B3LYP Hybrid Functional Fail for Metals? *J. Chem. Phys.* **2007**, *127*, 024103.

(40) Sun, Y.; Fournier, R.; Zhang, M. Structural and Electronic Properties of 13-atom 4d Transition-Metal Clusters. *Phys. Rev. A: At, Mol, Opt. Phys.* **2009**, *79*, 043202.

(41) Fouqueau, A.; Casida, M.; Daku, L.; Hauser, A.; Neese, F. Comparison of Density Functionals for Energy and Structural Differences Between the High-[⁵T_{2g}:(t_{2g})⁴(e_g)²] and Low-[¹A_{1g}:(t_{2g})⁶(e_g)⁰] spin states of iron(II) coordination compounds. II. More functionals and the hexaminoferrous cation, [Fe(NH₃)₆]²⁺. *J. Chem. Phys.* **2005**, *122*, 044110.

(42) Adamo, C.; Barone, V. Toward Reliable Density Functional Methods without Adjustable Parameters: The PBE0 Model. *J. Chem. Phys.* **1999**, *110*, 6158–6170.

(43) Perdew, J.; Ernzerhof, M.; Burke, K. Rationale for Mixing Exact Exchange with Density Functional Approximations. *J. Chem. Phys.* **1996**, *105*, 9982–9985.

(44) Marsman, M.; Paier, J.; Stroppa, A.; Kresse, G. Hybrid Functionals Applied to Extended Systems. *J. Phys.: Condens. Matter* **2008**, *20*, 064201.

(45) Paier, J.; Hirschl, R.; Marsman, M.; Kresse, G. The Perdew-Burke-Ernzerhof Exchange-Correlation Functional Applied to the G2–1 Test Set Using a Plane-Wave Basis Set. *J. Chem. Phys.* **2005**, *122*, 234102.

(46) Han, J.; Zhao, R.; Duan, Y. Geometries, Stabilities, and Growth Patterns of the Bimetal Mo₂-doped Si_n (n = 9–16) Clusters: A Density Functional Investigation. *J. Phys. Chem. A* **2007**, *111*, 2148–2155.

(47) Wang, J.; Liu, J. Investigation of Size-Selective Zr₂@Si_n (n = 16–24) Caged Clusters. *J. Phys. Chem. A* **2008**, *112*, 4562–4567.

(48) Gunaratne, K.; Berkdemir, C.; Harmon, C.; Castleman, A. Probing the Valence Orbitals of Transition Metal-Silicon Diatomic Anions: ZrSi, NbSi, MoSi, PdSi and WSi. *Phys. Chem. Chem. Phys.* **2013**, *15*, 6068–6079.

(49) Choi, K.; Choi, S.; Ahn, D.; Han, S.; Kang, T.; Baek, S.; Kim, S. J. Clustering Dynamics of the Metal-Benzene Sandwich Complex: The Role of Microscopic Structure of the Solute In the Bis(η⁶-benzene) chromium ·Ar_n Clusters (n = 1–15). *J. Phys. Chem. A* **2008**, *112*, 7125–7127.

(50) Koyasu, K.; Atobe, J.; Furuse, S.; Nakajima, A. Anion Photoelectron Spectroscopy of Transition Metal- and Lanthanide Metal-Silicon Clusters: MSi_n[−] (n = 6–20). *J. Chem. Phys.* **2008**, *129*, 214301.